analytical chemistry

pubs.acs.org/ac Article

Oxygen Vacancy-Enhanced Electrochemiluminescence Sensing Strategy Using Luminol Thermally Encapsulated in Apoferritin as a Transducer for Biomarker Immunoassay

Yu Du, Jingwei Xue, Xu Sun, Dan Wu, Xuejing Liu, Huangxian Ju, Lei Yang,* and Qin Wei*

Cite This: *Anal. Chem.* 2020, 92, 8472−8479 Read Online

ACCESS | Metrics & More | Article Recommendations | Supporting Information

ABSTRACT: Oxygen vacancies (OVs) enhanced electrochemiluminescence (ECL) biosensing strategy using luminol thermally encapsulated in apoferritin (Lum@apoFt) as an efficient transducer was investigated for ultrasensitive biomarker detection. By applying the oxygen-defect engineering (ODE) strategy, the OVs enriched cobalt−iron oxide (r-$CoFe_2O_4$) was fabricated as the sensing substrate to boost the electron mobility and catalyze the generation of superoxide anion radical ($O_2^{\bullet-}$) for signal amplification. It should be noted that r-$CoFe_2O_4$ with higher OVs density dramatically accelerated the ECL reaction between $O_2^{\bullet-}$ and luminol anionic radicals, achieving 6.5-fold stronger ECL output than $CoFe_2O_4$ with no or low OVs density. Moreover, facile encapsulation of approximate 412 luminol molecules in a single apoFt cavity was first realized by an efficient thermal-induction method. The obtained Lum@apoFt complexes exhibited well-maintained ECL efficiency and excellent biocompatibility for biological modifications. On this basis, a biosensor was developed for early diagnostics of squamous cell carcinomas by detecting its representative biomarker named cytokeratin 19 fragment 21-1 (CYFRA 21-1), from which excellent linearity was achieved in 0.5 pg/mL to 50 ng/mL with a detection limit of 0.14 pg/mL. This work not only put forward a novel idea of creating OVs enriched sensing interface with excellent signal-amplification function but also proposes a facile and robust methodology to design apoFt-based transducers for developing more practical nanoscale biosensors in early diagnostics of diseases.

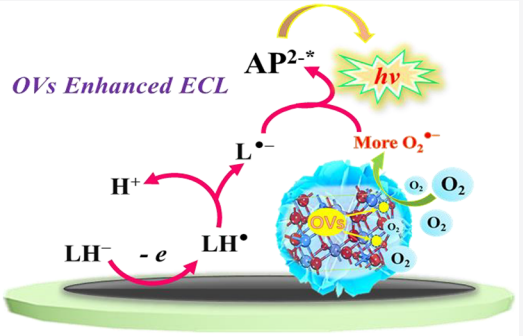

INTRODUCTION

Biosensors, known as sensing devices that can convert specific biorecognition events into detectable signals, has gained substantial attention in analyzing targets like pathogens, toxins, antigens, and nucleic acids.[1−5] In biosensor constructions, the successful application of a powerful sensing technique is of paramount importance in achieving excellent performances.[6] Considering the merits of high sensitivity, wide dynamic range, spatial controllability, and facility, electrochemiluminescence (ECL) technique based biosensors have been extensively established for biomarker detection in real samples.[7] Strikingly, surface modification of advanced nanomaterials on glassy carbon electrode (GCE) can incredibly enhance the electrical conductivity, catalytic activity, and biocompatibility to achieve the excellent signal-amplifying capability of biosensors.[1,2] Moreover, widespread participation of excellent ECL luminophores like ruthenium(III) complexes, iridium(III) complexes, luminol, and its derivatives has made it more facile and efficient to develop more innovative signal transducers for biosensor fabrications.[7−11] Despite the pioneering developments in biosensing techniques, effective and innovative strategies are still highly demanded to accelerate the groundbreaking progress of biosensors with higher reliability and wider clinical applications.

Transition-metal oxides with appealing catalytic activity, high abundance, physicochemical stability, and low toxicity have recently attracted significant attention in electro-catalysis, energy materials, and batteries.[12−16] Nevertheless, their biosensing applications are limited due to the inferior electrochemical properties.[12,17] To date, the oxygen-defect engineering (ODE) strategy has been advocated in creating oxygen vacancies (OVs) on the surfaces of transition-metal oxides, which remarkably improved the electrical and catalytic properties.[12,14] Inspired by this, we first introduced ODE strategy to build a highly efficient OVs enhanced sensing interface for ECL amplification. Through a controllable solid-state reaction using $NaBH_4$ as an oxygen scavenger, abundant OVs were created on the nanosurface of cobalt−iron oxide (r-$CoFe_2O_4$).[12] The crucial role of OVs in enhancing the ECL emission was revealed by employing a traditional luminol-based ECL system using the dissolved O_2 as a nontoxic

Received: March 21, 2020
Accepted: May 22, 2020
Published: May 22, 2020

https://dx.doi.org/10.1021/acs.analchem.0c01238
Anal. Chem. 2020, 92, 8472−8479

Scheme 1. Preparation Process of r-$CoFe_2O_4$–HWR substrate (A), Lum@apoFt-Ab_2 Bioconjugate and the Proposed ECL Biosensor for CYFRA 21-1 Detection (C)

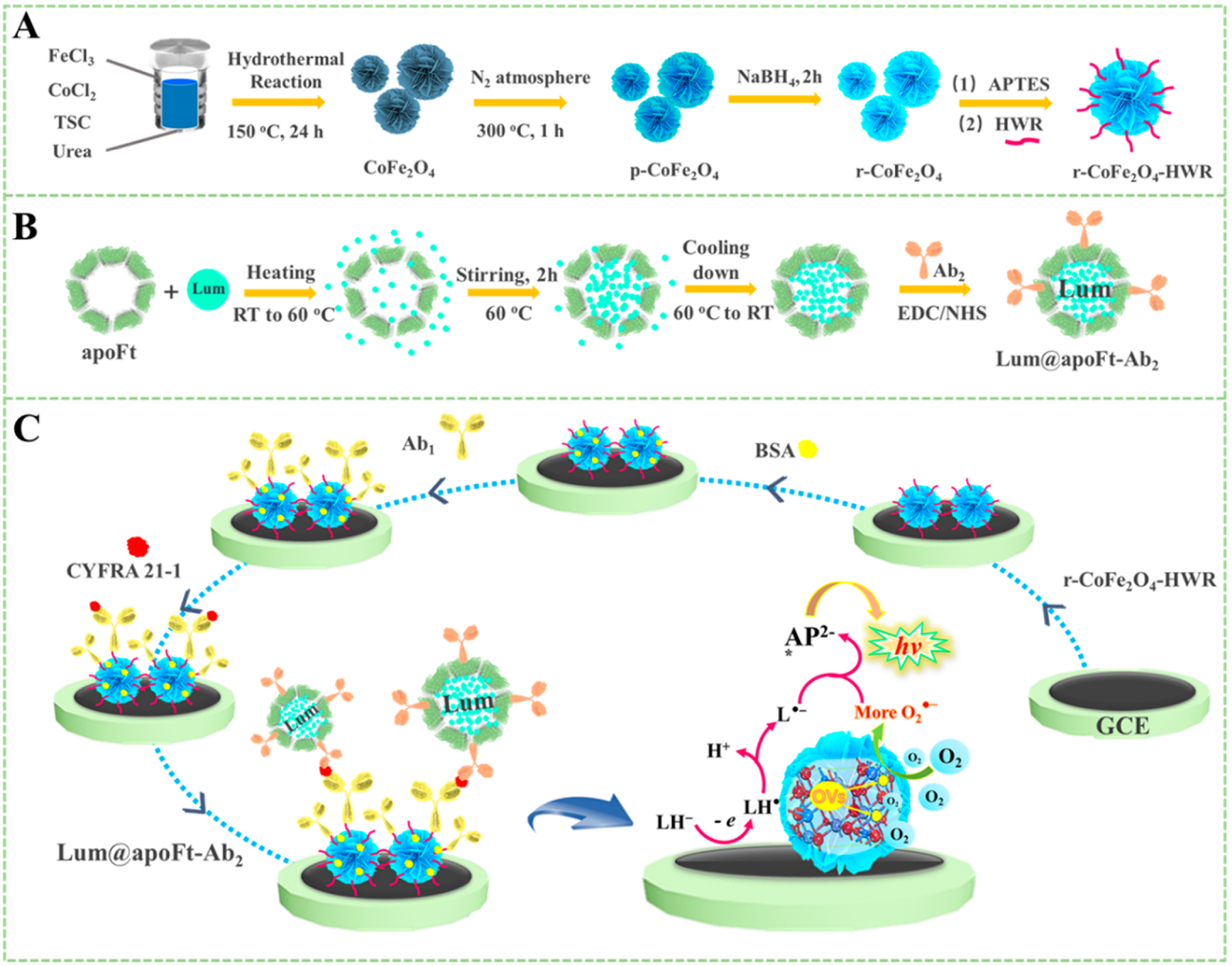

coreactant. Compared with pristine $CoFe_2O_4$ and $CoFe_2O_4$ with low OVs(p-$CoFe_2O_4$), the r-$CoFe_2O_4$ was demonstrated that can dramatically accelerate the ECL reaction between $O_2^{\bullet-}$ and luminol anionic radicals to achieve 6.5-fold stronger ECL output, revealing the advances of r-$CoFe_2O_4$ modified GCE as the sensing element in the biosensor construction.

Ferritin (Ft), which is composed of 24 protein subunits and one ferric nanocore, has been universally studied in nanomaterial science due to its superiorities of uniform size, enzyme-mimic activity, biocompatibility, pH tolerance, and thermal stability.[18,19] Recently, modifications of luminol and biomolecules on the outer surface of Ft have been achieved for biosensing.[20,21] However, the potential problem was found existed during the modification process. It should be noticed that the binding competition between these two species is subsistent, which can decrease the binding ratio of each other and mutually interfered with their normal functions during the sensing process. To better perform their functions in separate positions, an effective strategy which combines inner encapsulation of luminophores and outer modification of antibodies is first proposed by using apoferritin (apoFt), Ft that devoid of ferric nanocore, as the nanocarrier.[22] It is worth noticing that apoFt provides a homogeneous cavity for encapsulating luminol molecules, and antibodies can be easily decorated on the outer surface due to the abundant amino groups.[23] Previously, large molecules like uranyl acetate dihydrate, phosphotungstic acid, doxorubicin have been proved that can enter into apoFt cavity through the 3–4 Å channels between subunits at room temperature (RT).[24,25] To make the encapsulation process more efficient, herein, a thermally induced channel expansion/contraction method was proposed. Impressively, this facile strategy not only accelerated the encapsulation rate of luminol in apoFt (Lum@apoFt) with well- maintained ECL efficiency but also reserved the biological function of nanocage for antibody modifications, thus offering a newly designed signal transducer for ECL biosensor construction.

In view of the above, a highly efficient ECL biosensor was developed for biomarkers detection by using r-$CoFe_2O_4$ as the sensing substrate and Lum@apoFt as the signal transducer. Before incubating the capture-antibody (Ab_1), site-directed Fc binding heptapeptide HWRGWVC (HWR) was conjugated with r-$CoFe_2O_4$ via amide bonds to increase the interfacial specificity toward antigen.[19,26] After the modification of detection antibody (Ab_2) labeled Lum@apoFt (Lum@apoFt-Ab_2) bioconjugate, a sandwich-type immunocomplex was formed. Benefiting from the OVs induced ECL amplification effect, the biorecognition between Ab_2 and target antigen can

https://dx.doi.org/10.1021/acs.analchem.0c01238
Anal. Chem. 2020, 92, 8472–8479

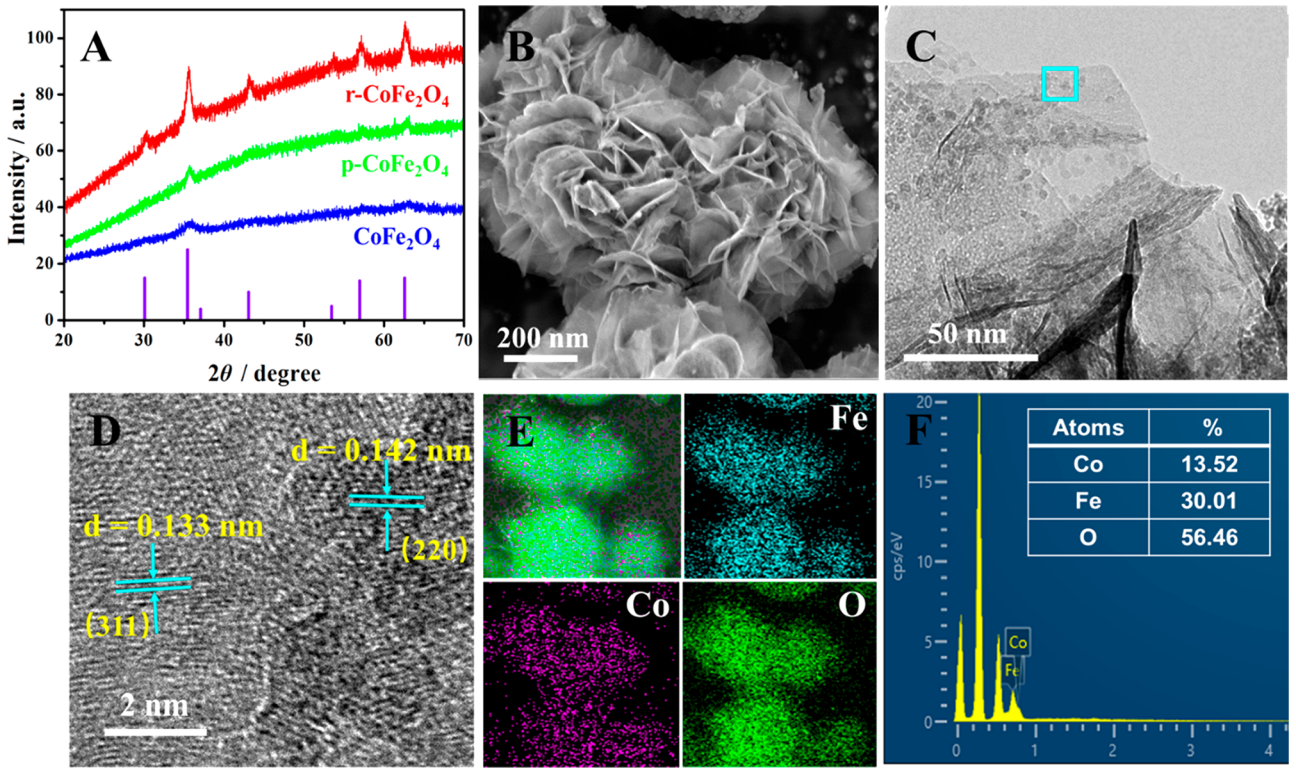

Figure 1. (A) XRD patterns of $CoFe_2O_4$, p-$CoFe_2O_4$, and r-$CoFe_2O_4$. The SEM image (B), TEM image (C), HRTEM image (D), SEM elemental mapping (E), and EDS (F) of r-$CoFe_2O_4$.propyl)-3-ethyl carbodiimide hydrochloride (EDC) and *N*-hydroxysuccinimide (NHS) solution at 25 °C for 30 min. After centrifugation, the obtained r-$CoFe_2O_4$–HWR solution stored at 4 °C for electrode modifications.

be effectively transduced into remarkably amplified ECL signals, thus different concentrations of antigens can be sensitively quantified. Moreover, satisfying accuracy and practicability of the developed biosensor were well demonstrated using cytokeratin 19 fragment 21-1(CYFRA 21-1), a reliable biomarker for early diagnostics of squamous cell carcinomas,[27−30] as the real antigen target. To the best of our knowledge, the innovative combination of OVs enhanced ECL biosensing and thermally induced luminol encapsulation in apoFt has never been reported before, thus highlighting its significances in providing new insights of constructing OVs enriched sensing substrates and designing apoFt-based efficient transducers for ultrasensitive ECL biosensing of biomarkers in real samples.

EXPERIMENTAL SECTION

Preparation of $CoFe_2O_4$, p-$CoFe_2O_4$, and r-$CoFe_2O_4$. This preparation (Scheme 1A) was conducted with the reference of a reported method.[12] 2.8 mmol urea (CH_4N_2O) and 0.02 mmol trisodium citrate (TSC) were uniformly dissolved into 80 mL of deionized water. Then, with the following addition of 0.8 mmol $FeCl_3{\cdot}6H_2O$ and 0.4 mmol $CoCl_2{\cdot}6H_2O$ into the above solution, the resultant mixture was stirred for 2 h at room temperature. After that, the mixture was transferred into a 100 mL Teflon-lined autoclave for 24 h of reaction at 150 °C. When the reaction finished, the autoclave was cooled to RT, and the product was centrifuged and washed at least three times. After drying in a 50 °C vacuum, the pristine $CoFe_2O_4$ was finally acquired. To prepare the p-$CoFe_2O_4$, the pristine $CoFe_2O_4$ was annealed in N_2 atmosphere at 300 °C for 1 h. To further prepare the r-$CoFe_2O_4$, 100 mg of p-$CoFe_2O_4$ was dispersed into 80 mL of 10 M of $NaBH_4$ with the assistance of 3 h of ultrasonication at room temperature. The resultant black product was collected by centrifugation and three times of washing with water and ethanol. Finally, the solid product f r-$CoFe_2O_4$ was dried in a vacuum.

Preparation of r-$CoFe_2O_4$–HWR. First, 10 mg of r-$CoFe_2O_4$ was immersed into 1 mL of ethanol containing 5% APTES and kept at 4 °C overnight to generate amino groups on the surface. After centrifugation and washing with ethanol for three times, 50 μg of HWR was mixed with 1 mL r-$CoFe_2O_4$ solution (2 mg/mL) with the assistance of 20 mmol of freshly prepared 1-(3-(dimethylamino)

Preparation of Lum@apoFt-Ab_2. As shown in Scheme 1B, 1 mL of luminol solution (3 mmol/L) was mixed with 5 nmol of apoFt for 15 min of stirring at RT to obtain a uniform mixture. Then, the temperature was slowly adjusted up to 60 °C. After continuous stirring for another 2h, the solution temperature slowly came down to RT to end the preparation process. The apoFt channels will expand along with the uprising of temperature, thus allowing more luminol molecules to enter into the apoFt cavity by the thermal diffusion. As the temperature came down, the channels will contract and the luminol molecules will be encapsulated in apoFt.

Fabrication Process of Biosensor. As shown in Scheme 1C, bare GCE was carefully polished with different sizes of slurry polishing powder. After ultrasonic cleaning with ethanol and ultrapure water for three times, the resultant GCE was dried under N_2 atmosphere. First,10 μL of r-$CoFe_2O_4$–HWR solution (2 mg/mL) was modified onto the bare GCE surface. Then, 3 μL of BSA (2%) was coated on its surface to block the nonspecific binding sites to ensure the site-oriented capture of Ab_1 by r-$CoFe_2O_4$–HWR, after which 10 μL of Ab_1 solution

https://dx.doi.org/10.1021/acs.analchem.0c01238
Anal. Chem. 2020, 92, 8472−8479

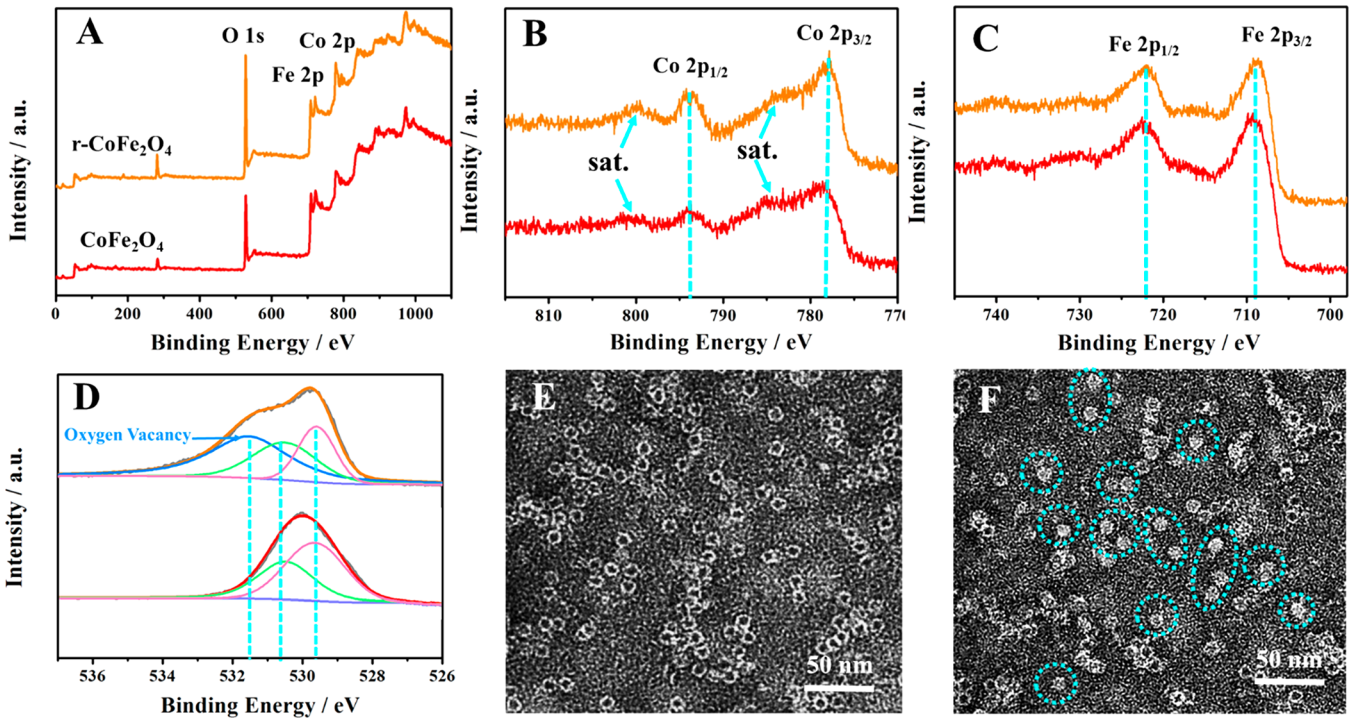

Figure 2. (A) XPS spectrum of $CoFe_2O_4$ and r-$CoFe_2O_4$ (A), and the core level spectra of Co 2p (B), Fe 2p (C), and O 1s (D). TEM image of apoFt and the prepared Lum@apoFt.

(100 μg/mL) was incubated for 1 h at 4 °C. After incubating 10 μL of CYFRA 21-1 antigen solution, 10 μL of Lum@apoFt-Ab_2 was modified to fabricate the sandwich-like immunocomplex. Notably, the electrode surface will be mildly rinsed with PBS (pH 7.4) solution to get rid of the unabsorbed biomolecules after each modifying step. In this way, the biosensor was completely established for the ECL measurements that conducted in an MPI-F flow-injection ECL detector accompanied by an electrochemical workstation.

RESULTS AND DISCUSSION

Characterizations of r-$CoFe_2O_4$ and Lum@apoFtBioconjugate. Powerful techniques were utilized to characterize the structural, morphological, and elemental composition information of r-$CoFe_2O_4$ composite. In Figure 1A, the X-ray diffraction (XRD) pattern isdisplayed to characterize the crystal structure of $CoFe_2O_4$, p-$CoFe_2O_4$, and r-$CoFe_2O_4$, from which all the diffraction peaks are found well-matched with $CoFe_2O_4$ (JCPDS Card No. 79-1744), indicating that OVs have no influence on the crystal structure of $CoFe_2O_4$. In Figure 1B, the scanning electron microscope (SEM) image of r-$CoFe_2O_4$ shows a better defined flower-like structure than that of $CoFe_2O_4$ and p-$CoFe_2O_4$ (Supporting Information (SI) Figure S1), which is further confirmed by the transmission electron microscope (TEM) image in Figure 1C. The high-resolution TEM (HRTEM) image in Figure 1D shows two spacing distances of 0.133 and 0.142 nm, which are corresponded to (311) and (220) crystal planes of $CoFe_2O_4$, respectively. Besides, the elemental mapping images in Figure 1E exhibits the elemental composition and even distribution of r-$CoFe_2O_4$. In Figure 1F, the atom ratio of Co, Fe, O elements from the energy-dispersive X-ray spectroscopy (EDS) is determined to be 1:2.21:4.17, further demonstrating the formation of $CoFe_2O_4$ phase. Moreover, the Fourier transform infrared (FT-IR) spectroscopy (SI Figure S2) are provided to prove the successful amine functionalization of r-$CoFe_2O_4$.

X-ray photoelectron spectra (XPS) pattern is provided to confirm the valence states of r-$CoFe_2O_4$ and the existence of oxygen vacancies by comparing it with pristine $CoFe_2O_4$. In Figure 2A, the XPS data of $CoFe_2O_4$ and r-$CoFe_2O_4$ are provided. As for the core level spectra of Co 2p in Figure 2B, the peaks that situated at 794.1 and 778.9 eV are assigned to the Co $2p_{1/2}$ and Co $2p_{3/2}$, respectively. Because there are two satellite peaks that appeared at 803.1 and 785.2 eV, the valence of Co is designated as +2 in the composite. Looking at the core level spectra of Fe 2p in Figure 2C, two characteristic peaks can be clearly seen at 722.7 and 709.3 eV, which indicates that the valence of Fe is +3. Moreover, the O 1s core-level spectra in Figure 2D displays two typical peaks at 530.2 and 529.6 eV, which are attributed to oxygen in hydroxyl groups and metal−oxygen bonds, respectively.[12] As can be further seen in Figure 2D, the shoulder peak located at 531.3 eV is attributed to the defect sites with low oxygen coordination, revealing that the oxygen vacancies have been created on the $CoFe_2O_4$ surface.[13,16]

Considering the inner surface of apoFt is rich in acidic residues like Glu and Asp, the generated high negative charge density makes it more convenient to immobilize the positively charged luminol molecules inside of the cavity.[25] After employing the UV−vis spectra demonstration in SI Figure S3 to prove the successful preparation of Lum@apoFt, TEM was further utilized to characterize the microcosmic morphologies of apoFt and Lum@apoFt using amine molybdate solution (3%, pH 7.4) as the negative staining reagent. Comparing with the TEM image of apoFt (Figure 2E), it can be clearly observed that the Lum@apoFt (Figure 2F) exhibits a similar spherical morphology, indicating the thermally induced encapsulation had negligible effects on the nanocage morphology. Because the amine molybdate mole-

https://dx.doi.org/10.1021/acs.analchem.0c01238
Anal. Chem. 2020, 92, 8472−8479

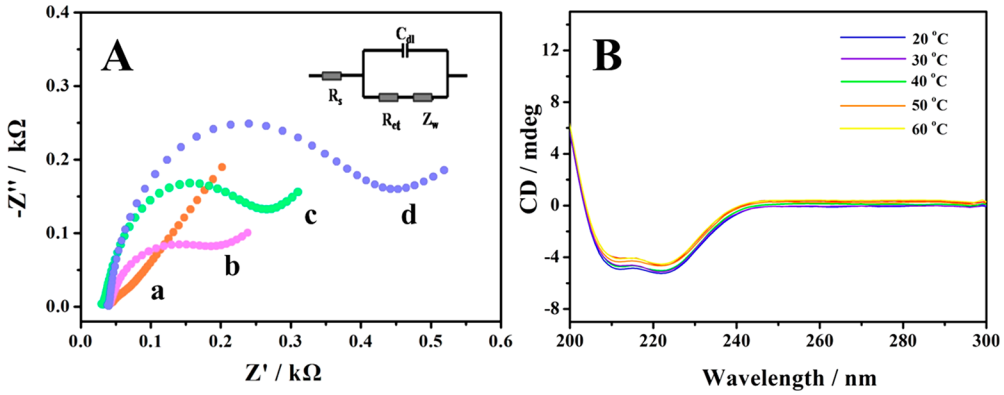

Figure 3. (A) the EIS spectra of bare GCE (curve a), r-$CoFe_2O_4$ (curve b), p-$CoFe_2O_4$ (curve c), and $CoFe_2O_4$ (curve d). (B) the CD spectra of apoFt solution at different temperatures (20−60 °C).

cules penetrated in apoFt through the channels, "black" molybdate cores appeared inside of the apoFt.[24] However, most of the apoFt exhibits full "white" cores after the encapsulation of luminol molecules because the amine molybdate molecules could not get into the apoFt. Due to the occupation of luminol molecules, the successful preparation of Lum@apoFt using the proposed thermal strategy.

Increased Electroactive Surface Area of r-$CoFe_2O_4$. To demonstrate that $CoFe_2O_4$ with higher OVs density can dramatically enhance the electrochemical behavior of the sensing interface, the electro-active surface area of $CoFe_2O_4$, p-$CoFe_2O_4$, and r-$CoFe_2O_4$ modified GCEs were scanned by cyclic voltammetry (CV) using $[Fe(CN)_6]^{4-/3-}$ as the redox probe. In terms of the commonly used Randles-Sevcik equation:[11,31]

$$I_p = 2.69 \times 10^5 AD^{1/2} n^{3/2} v^{1/2} c$$

where the I_p stands for the peak reduction current appears during the scanning process, A is the electroactive surface area (cm^2) that will be determined, D is the diffusion coefficient of $[Fe(CN)_6]^{4-/3-}$ whose value can be determined to be $6.70 \pm 0.02 \times 10^{-6}$ cm^2 s^{-1} at 25 °C, v is the CV scanning rate (V/s), and c is the concentration of the $K_3Fe(CN)_6$(5 mmol/L), n is the number of electrons that transported during oxidation−reduction reaction (n = 1). After scanning these electrodes at different rates, regression equations of pure $CoFe_2O_4$ (SI Figure S4A), p-$CoFe_2O_4$ (SI Figure S4B) and r-$CoFe_2O_4$ (SI Figure S4C) modified electrodes are presented as $I = 522.35 \times v^{1/2} + 127.11$ (R^2 = 0.982), $I = 626.27 \times v^{1/2} + 155.29$ (R^2 = 0.991) and $I = 987.44 \times v^{1/2} + 132.99$ (R^2 = 0.989), respectively. Correspondingly, the electro-active surface areas were calculated to be 15.00 mm^2, 21.99 mm^2, and 28.36 mm^2, respectively, indicating the increased the electro-active surface area by the OVs generated by the ODE strategy.

Electrochemical Impedance Spectroscopy (EIS) Studies. Though the narrower bandgap of r-$CoFe_2O_4$ endowed itself with faster electron-transfer ability than the p-$CoFe_2O_4$ (SI Figure S5), the enhanced interfacial electron transfer by OVs was further explored by EIS. The EIS data of electrodes modified with 2 mg/mL of $CoFe_2O_4$, p-$CoFe_2O_4$, and r-$CoFe_2O_4$ were tested in 5 mmol/L of $[Fe(CN)_6]^{3-/4-}$ solution, whose charge transfer resistance (R_{ct}) data were presented in Figure 3A. The R_{ct} value of r-$CoFe_2O_4$ (curve b) modified electrode is much smaller than that of p-$CoFe_2O_4$ (curve c) and $CoFe_2O_4$ (curve d) modified electrodes, which indicates that the higher OVs density can efficiently accelerate the electron transfer on the sensing interface. Using r-$CoFe_2O_4$ as the ECL sensing substrate is quite beneficial to boosting the interfacial electron transfer for better performance of biosensor. Besides, EIS was also employed to characterize the stepwise fabrication of the biosensor in SI Figure S6.

Superiorities of apoFt in luminol Immobilization. To prove the improved loading capacity of luminol molecules, high-performance liquid chromatography (HPLC) test was conducted on an Agilent 1260 HPLC system consisting of a UV detector and a Zorbax C18 column (4.6 × 250 mm, 5 μm) using a mobile phase of acetonitrile/water (60:40, v/v). The Lum@Ft solution was obtained by using 5 nmol of Ft to cross-link with 1 mL of luminol (3 mmol/L) via glutaraldehyde under room temperature, then the Lum@apoFt solution was obtained by mixing apoFt with 1 mL of luminol (3 mmol/L) for stirring at 60 °C. After ultrafiltration, filtrates (1 mL) of Lum@apoFt and Lum@Ft were collected for the HPLC test, the peak areas of which were found to be 169.7 and 328.9 mAU*s, respectively. According to the HPLC calibration curve of standard luminol solutions with concentration from 0.1 mmol/L to 5 mmol/L (SI Figure S7), the corresponding concentration values of the above were calculated to be 0.94 mmol/L and 1.96 mmol/L. Therefore, the loading capacities of single Ft and apoFt were determined averagely to be 412 and 208 luminol molecules, respectively. Moreover, the reproducibility of this proposed thermally induced encapsulation method was proved by the *intra* and *inter*assays (SI Figure S8), whose SD values were calculated to be 4.40% and 5.68%, respectively. The results highlighted the advance of apoFt in loading larger amounts of luminol via the internal encapsulation method.

As well-known, pH-induced disassembly/reassembly is regarded as the most conventional pathway to encapsulate molecules or ions in apoFt for biosynthesis and applications.[24] However, extremely acid/alkaline conditions might destroy the functional groups on the nanocage, thus decreasing its biocompatibility for bioanalysis, especially for the outer biomodifications.[25] To conquer this limitation, a thermally induced strategy was first brought up to include luminol molecules inside of apoFt without dramatic pH adjustments. To prove the thermal stability of apoFt under 60 °C, circular dichroism (CD) data of the Lum@apoFt samples prepared under temperatures from 20 to 60 °C for 1 h were recorded by scanning from 200 to 300 nm utilizing a MOS-450 spectrometer consisting of a quartz cuvette of 1 mm optical path length at 25 °C. As shown in Figure 3B, negligible

https://dx.doi.org/10.1021/acs.analchem.0c01238
Anal. Chem. 2020, 92, 8472−8479

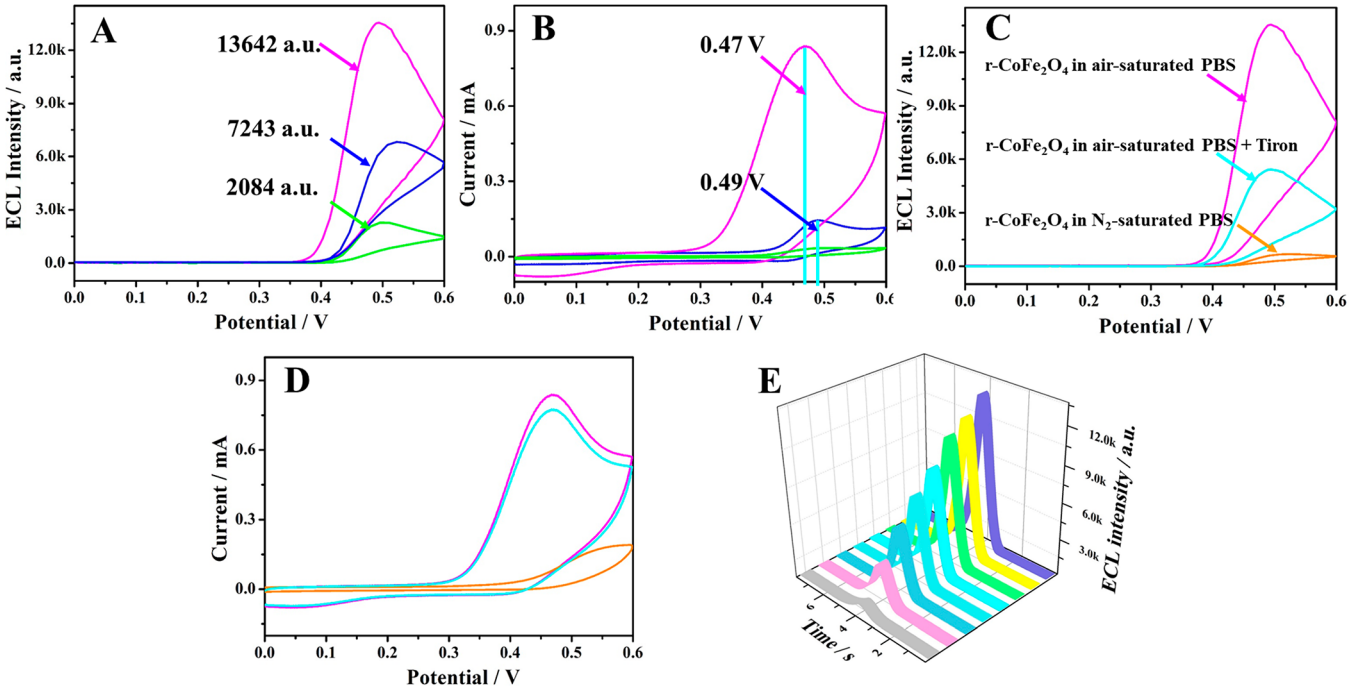

Figure 4. ECL intensity-potential curves (A) and their corresponding CV curves (B) of $CoFe_2O_4$, p-$CoFe_2O_4$, and r-$CoFe_2O_4$ modified electrodes detected in 0.5 mmol/L of air-saturated luminol solution. The ECL intensity-potential curves (C) and the corresponding CV curves (D) of r-$CoFe_2O_4$ modified electrode detected in 0.5 mmol/L of luminol solution with different treatments. (E) ECL intensity-time curves for CRYRA 21-1 with concentrations of 0.5 pg/mL, 5 pg/mL, 50 pg/mL, 500 pg/mL, 1 ng/mL, 10 ng/mL, 20 ng/mL, and 30 ng/mL.

variation was found, proving the favorable thermal stability of apoFt under 60 °C. Thus, the feasibility of this method is well demonstrated.

Discussions of Signal Amplification and Luminous Mechanism. To investigate the signal amplification of the OVs involved ECL emission of luminol-dissolved O_2 system, electrodes modified with 10 μL of 2 mg/mL $CoFe_2O_4$, p-$CoFe_2O_4$, and r-$CoFe_2O_4$ were detected in air-saturated PBS (pH 8.2) containing 0.5 mmol/L of luminol, respectively. As shown in Figure 4A, the r-$CoFe_2O_4$ modified electrode (magenta curve) achieved the maximum ECL intensity among the samples. By comparing $CoFe_2O_4$ (green curve) with p-$CoFe_2O_4$ (blue curve), it can be concluded that the existence of OVs can enhance the ECL signal of luminol. By comparing p-$CoFe_2O_4$ (blue curve) with r-$CoFe_2O_4$ (magenta curve), it can be concluded that higher OVs concentration can further boost the ECL process with stronger intensity. According to the corresponding CV curves in Figure 4B, it can be seen that the r-$CoFe_2O_4$ (magenta curve) owns a negatively shifted anodic potential (0.47 V) and a greatly increased anodic current, which means that $CoFe_2O_4$ with higher OVs density not only decreased the overpotential of the redox reaction between luminol and O_2 but also promoted the current intensity, thus dramatically enhancing the ECL performance of the biosensor during the detection.

To have a better understanding of the luminous mechanism, two possible arguments are proposed: (1) The OVs can serve as the adsorption and reaction sites of dissolved O_2 and then facilitate the electron transport to catalyze the generation of $O_2^{\bullet-}$ for the ECL reaction. (2) The OVs can serve as the adsorption site for H_2O molecules, and then electro-catalyze the generation of more O_2 as coreactant via the oxygen evolution reaction (OER) process. To demonstrate the above, the r-$CoFe_2O_4$ electrodes were further detected in N_2-satuated PBS. Nevertheless, luminol can hardly generate ECL signals in the N_2-saturated environment (Figure 4C). As shown in Figure 4C, the ECL intensity of r-$CoFe_2O_4$ electrodes dramatically decreased after the addition of Tiron (1,2-dihydroxy-3,5-benzene disulfonic acid disodium salt), a specific $O_2^{\bullet-}$ scavenger.[32,33] This decrement was not caused by the electronic block on the electrode surface since the current only decreased a little in Figure 4D. Apparently, it was the $O_2^{\bullet-}$ elimination that decreased the ECL signal. Therefore, it can be included that the r-$CoFe_2O_4$ with higher OVs density can absorb dissolved O_2 on the interface and then catalyze the generation of more $O_2^{\bullet-}$ efficiently to react with luminol anionic radicals ($L^{\bullet-}$) that generated by the electrochemical oxidization of luminol anions (LH^-). In this way, more excited-state species of luminol (AP^{2-}*) can be produced to obtain greatly amplified signals (eq. 1−5).

$$LH^- - e^- \rightarrow L^{\bullet-} + H^+ \quad (1)$$

$$O_2 + e^- \rightarrow O_2^{\bullet-} \quad (2)$$

$$L^{\bullet-} + O_2^{\bullet-} \rightarrow LO_2^{2-} \quad (3)$$

$$LO_2^{2-} \rightarrow AP^{2-}* + N_2 \quad (4)$$

$$AP^{2-}* \rightarrow AP^{2-} + h\nu \quad (5)$$

Calibration Curve. Under optimized experimental conditions (SI Figure S9), the calibration relationship between ECL intensity and standard CFRRA 21-1 concentration was investigated. The developed ECL biosensor was used to detect standard CFRRA 21-1 samples of different concentrations in 10 mL of PBS (pH 8.2). As shown in SI Figure S10, it can be seen the ECL intensities of the biosensors were in an excellent linear relation with the logarithm of CFRRA 21-1 concentration (0.5 pg/mL to 50 ng/mL). The linear regression

https://dx.doi.org/10.1021/acs.analchem.0c01238
Anal. Chem. 2020, 92, 8472−8479

equation was expressed as $y = 2343.04 \times \log c + 8432.43$, $R^2 = 0.994$, and the detection limit is estimated to be 0.14 pg/mL ($S/N = 3$). Moreover, the corresponding ECL intensity-time curve of this linearity was shown in Figure 4E. Given that most of the methods for CFRRA 21-1 were using electrochemical sensors,[27−30] this first proposed ECL biosensor exhibited sparkling superiorities of linear range and detection limit by the comparison in Table 1.

Table 1. Comparison Between this Proposed Method and Other Reported Sensors for CYFRA 21-1 Detection

electrode materials	linear range (ng/mL)	detection limit (pg/mL)	ref
3D graphene-Au NPs	0.25 — 800	100	27
CeO_2 nanocube/RGO	6.25×10^{-4}— 0.01	0.625	29
ZrO_2-RGO	2 — 22	122	30
OVs enriched $CoFe_2O_4$	5×10^{-4}— 50	0.14	this work

Real Sample Analysis. Based on the favorable specificity, stability, and reproducibility of the biosensor (SI Figure S11), the standard addition method was used to evaluate the accuracy and practicality of the constructed ECL biosensor for CYFRA 21-1 analysis. Normal human serum was spiked with standard CYFRA 21-1 samples with different concentrations (0.1 ng/mL, 2 ng/mL, 10 ng/mL, and 30 ng/mL). Then, all the samples were detected by the developed biosensors. As shown in Table 2, the recovery data of the above were found

Table 2. Recovery Data of Normal Human Serum Spiked with Different Concentration of CYFRA 21-1

sample number	spiked concentration (ng/mL)	found (ng/mL), $n = 5$	recovery %
1	0.1	0.10, SD = 1.98%	103.00
2	2	1.91, SD = 2.69%	95.50
3	10	10.23, SD = 1.76%	102.30
4	30	29.22, SD= 3.12%	97.40

from 95.5% to 103.0%. Therefore, the accuracy and practicality of the proposed ECL biosensor were successfully proved, showing great potential in the early diagnostics of squamous cell carcinomas.

CONCLUSIONS

Conclusively, the OVs enhanced ECL biosensing strategy is successfully applied to fabricate a highly efficient biosensor for biomarker immunoassay. The r-$CoFe_2O_4$ with higher OVs density was fabricated as the biosensor substrate by the ODE strategy. In-depth characterization of the r-$CoFe_2O_4$ showed significant improvement in facilitating the interfacial electron-transfer and catalyzing the generation of $O_2^{\bullet-}$ in comparison to $CoFe_2O_4$ with low or no OVs density. With further introducing the site-oriented HWR linkers, the formed r-$CoFe_2O_4$−HWR substrate leads to high antibody binding specificity. Then, a novel thermally induced channel expansion method was first proposed and applied to design the biocompatible transducer of Lum@apoFt, which perfectly avoided the inevitable denaturation caused by the pH-induced disassembly/reassembly and complicated procedures in conventional apoFt-complex synthesis. Using the developed biosensor to monitor the concentration of CFRRA 21-1 in human serum, excellent linearity between 0.5 pg/mL and 50 ng/mL with a low detection limit of 0.14 pg/mL was achieved along with the favorable stability, specificity, and reproducibility. This work not only put forward new ideas of fabricating OVs enhanced sensing interface with excellent signal amplifying function, but also proposes a facile and robust methodology to design apoFt-based transducers in developing practical nanoscale biosensors for early diagnostics of diseases.

ASSOCIATED CONTENT

Supporting Information

The Supporting Information is available free of charge at https://pubs.acs.org/doi/10.1021/acs.analchem.0c01238.

Materials, reagents, apparatus, SEM images of pure $CoFe_2O_4$ and p-$CoFe_2O_4$, FT-IR spectra, UV−vis absorbance spectrum, the linear relation between the peak reduction current I and $v^{1/2}$, UV−vis diffuse reflectance spectra, EIS characterization, HPLC calibration curve, reproducibility of preparing Lum@apoFt, optimization of experimental conditions, the calibration curve of biosensor, specificity, stability, and reproducibility of biosensor (PDF)

AUTHOR INFORMATION

Corresponding Authors

Lei Yang − *Key Laboratory of Interfacial Reaction & Sensing Analysis in Universities of Shandong, School of Chemistry and Chemical Engineering, University of Jinan, Jinan 250022, PR China*; Phone: +86 531 82765730; Email: yanglei_19940831@163.com; Fax: +86 531 82765969

Qin Wei − *Collaborative Innovation Center for Green Chemical Manufacturing and Accurate Detection, University of Jinan, Jinan 250022, PR China*; orcid.org/0000-0002-3034-8046; Email: sdjndxwq@163.com

Authors

Yu Du − *Collaborative Innovation Center for Green Chemical Manufacturing and Accurate Detection, University of Jinan, Jinan 250022, PR China*

Jingwei Xue − *Key Laboratory of Interfacial Reaction & Sensing Analysis in Universities of Shandong, School of Chemistry and Chemical Engineering, University of Jinan, Jinan 250022, PR China*

Xu Sun − *Key Laboratory of Interfacial Reaction & Sensing Analysis in Universities of Shandong, School of Chemistry and Chemical Engineering, University of Jinan, Jinan 250022, PR China*; orcid.org/0000-0001-8762-4243

Dan Wu − *Key Laboratory of Interfacial Reaction & Sensing Analysis in Universities of Shandong, School of Chemistry and Chemical Engineering, University of Jinan, Jinan 250022, PR China*; orcid.org/0000-0002-8732-5988

Xuejing Liu − *Key Laboratory of Interfacial Reaction & Sensing Analysis in Universities of Shandong, School of Chemistry and Chemical Engineering, University of Jinan, Jinan 250022, PR China*

Huangxian Ju − *Collaborative Innovation Center for Green Chemical Manufacturing and Accurate Detection, University of Jinan, Jinan 250022, PR China*; orcid.org/0000-0002-6741-5302

Complete contact information is available at: https://pubs.acs.org/10.1021/acs.analchem.0c01238

https://dx.doi.org/10.1021/acs.analchem.0c01238
Anal. Chem. 2020, 92, 8472−8479

Notes

The authors declare no competing financial interest.

■ ACKNOWLEDGMENTS

This work was supported by the National Key Scientific Instrument and Equipment Development Project of China (No. 21627809); National Natural Science Foundation of China (No. 21777056), Special Foundation for Taishan Scholar Professorship of Shandong Province (No. ts201712052) Jinan Scientific Research Leader Workshop Project (2018GXRC024), the Innovation Team Project of Colleges and Universities in Jinan (No. 2019GXRC027).

■ REFERENCES

(1) Naylor, C. H.; Kybert, N. J.; Schneier, C.; Xi, J.; Romero, G.; Saven, J. G.; Liu, R.; Johnson, A. T. *ACS Nano* **2016**, *10* (6), 6173−6179.
(2) Fallatah, A.; Almomtan, M.; Padalkar, S. *ACS Sustainable Chem. Eng.* **2019**, *7* (9), 8083−8089.
(3) He, Y.; Xie, S.; Yang, X.; Yuan, R.; Chai, Y. *ACS Appl. Mater. Interfaces* **2015**, *7* (24), 13360−13366.
(4) Amiri, M.; Bezaatpour, A.; Jafari, H.; Boukherroub, R.; Szunerits, S. *ACS Sens.* **2018**, *3* (6), 1069−1086.
(5) Bickman, S. R.; Campbell, K.; Elliott, C.; Murphy, C.; O'Kennedy, R.; Papst, P.; Lochhead, M. J. *Environ. Sci. Technol.* **2018**, *52* (20), 11691−11698.
(6) Tung, N. H.; Chikae, M.; Ukita, Y.; Viet, P. H.; Takamura, Y. *Anal. Chem.* **2012**, *84* (3), 1210−1213.
(7) Xu, Z. H.; Wang, H.; Wang, J.; Zhao, W.; Xu, J. J.; Chen, H. Y. *Anal. Chem.* **2019**, *91* (18), 12000−12005.
(8) Liang, W.; Zhuo, Y.; Xiong, C.; Zheng, Y.; Chai, Y.; Yuan, R. *Biosens. Bioelectron.* **2017**, *94*, 568−574.
(9) Xing, H.; Zhai, Q.; Zhang, X.; Li, J.; Wang, E. *Anal. Chem.* **2018**, *90* (3), 2141−2147.
(10) Qiao, Y.; Li, Y.; Fu, W.; Guo, Z.; Zheng, X. *Anal. Chem.* **2018**, *90* (15), 9629−9636.
(11) Wang, H.; Yuan, Y.; Zhuo, Y.; Chai, Y.; Yuan, R. *Anal. Chem.* **2016**, *88* (4), 2258−2265.
(12) Guo, C.; Liu, X.; Gao, L.; Ma, X.; Zhao, M.; Zhou, J.; Kuang, X.; Deng, W.; Sun, X.; Wei, Q. *J. Mater. Chem. A* **2019**, *7* (38), 21704−21710.
(13) Zhang, B.; Wang, L.; Zhang, Y.; Ding, Y.; Bi, Y. *Angew. Chem., Int. Ed.* **2018**, *57* (8), 2248−2252.
(14) Zhang, L.; Fang, Q.; Huang, Y.; Xu, K.; Chu, P. K.; Ma, F. *Anal. Chem.* **2018**, *90* (16), 9821−9829.
(15) Gao, R.; Li, Z.; Zhang, X.; Zhang, J.; Hu, Z.; Liu, X. J. A. C. *ACS Catal.* **2016**, *6*, 400−406.
(16) Bao, J.; Zhang, X.; Fan, B.; Zhang, J.; Zhou, M.; Yang, W. L.; Hu, X.; Wang, H.; Pan, B. C.; Xie, Y. *Angew. Chem., Int. Ed.* **2015**, *54* (25), 7399−7404.
(17) Zhuang, L.; Jia, Y.; He, T.; Du, A.; Yan, X.; Ge, L.; Zhu, Z.; Yao, X. *Nano Res.* **2018**, *11* (6), 3509−3518.
(18) Akanda, M. R.; Ju, H. *Anal. Chem.* **2018**, *90* (13), 8028−8034.
(19) Yang, L.; Fan, D.; Zhang, Y.; Ding, C.; Wu, D.; Wei, Q.; Ju, H. *Anal. Chem.* **2019**, *9*, 7145−7152.
(20) Yang, L.; Jia, Y.; Wu, D.; Zhang, Y.; Ju, H.; Du, Y.; Ma, H.; Wei, Q. *Anal. Chem.* **2019**, *91* (21), 14066−14073.
(21) Yang, L.; Xue, J.; Jia, Y.; Zhang, Y.; Wu, D.; Ma, H.; Wei, Q.; Ju, H. *Biosens. Bioelectron.* **2019**, *142*, 111562.
(22) Günther, J.; Patrick, V. R.; Barbara, S. M.; Alexander, B. K. *Chem. Rev.* **2015**, *115* (4), 1653.
(23) Dostalova, S.; Cerna, T.; Hynek, D.; Koudelkova, Z.; Vaculovic, T.; Kopel, P.; Hrabeta, J.; Heger, Z.; Vaculovicova, M.; Eckschlager, T.; Stiborova, M.; Adam, V. *ACS Appl. Mater. Interfaces* **2016**, *8* (23), 14430−14441.
(24) Yang, R.; Tian, J.; Liu, Y.; Yang, Z.; Wu, D.; Zhou, Z. *J. Agric. Food Chem.* **2017**, *65* (46), 9950−9955.
(25) Zhang, S.; Zang, J.; Chen, H.; Li, M.; Xu, C.; Zhao, G. *Small* **2017**, *13* (37), 1701045.
(26) Yang, H.; Gurgel, P. V.; Williams, D. K., Jr.; Bobay, B. G.; Cavanagh, J.; Muddiman, D. C.; Carbonell, R. G. *J. Mol. Recognit.* **2009**, *23* (3), 271−282.
(27) Zeng, Y.; Bao, J.; Zhao, Y.; Huo, D.; Chen, M.; Yang, M.; Fa, H.; Hou, C. *Talanta* **2018**, *178*, 122−128.
(28) Chen, M.; Hou, C. J.; Hou, D. Q.; Yang, M.; Fa, H. B. *Anal. Methods* **2015**, *7*, 9466−9473.
(29) Pachauri, N.; Dave, K.; Dinda, A.; Solanki, P. R. *J. Mater. Chem. B* **2018**, *6*, 3000.
(30) Kumar, S.; Sharma, J. G.; Maji, S.; Malhotra, B. D. *Biosens. Bioelectron.* **2016**, *78*, 497−504.
(31) Li, L. L.; Liu, K. P.; Yang, G. H.; Wang, C. M.; Zhang, J. R.; Zhu, J. J. *Adv. Funct. Mater.* **2011**, *21* (5), 869−878.
(32) Huang, L.; Li, Z.; Zhang, D.; Li, H.; Shi, C.; Zhang, P.; Su, X.; Zhang, X. *Anal. Chem.* **2018**, *90* (21), 12971−12978.
(33) Xu, X.; Thompson, L. V.; Navratil, M.; Chemistry, E. A. A. J. A. *Anal. Chem.* **2010**, *82* (11), 4570−4576.

https://dx.doi.org/10.1021/acs.analchem.0c01238
Anal. Chem. 2020, 92, 8472−8479